Chemical Engineering Journal 540 (2026) 177655

Contents lists available at ScienceDirect

Chemical Engineering Journal

journal homepage: www.elsevier.com/locate/cej

A multi-functional passive fixation lead for diagnosis and treatment of cardiac diseases

Xuandi Deng [a,1], Yiran Hu [b,c,1], Puqing Yao [a,1], Chunhong Yu [a], Juwei Yang [c], Ruizeng Luo [d,e], Sijing Cheng [c], Hao Huang [c], Peng Cheng [f], Lei Jia [a], Xingyao Lv [a], Menghan Li [a], Zetao Zhao [a], Wei Hua [c], Yongjun Wang [b,g], Zhuo Liu [a,**], Zhou Li [d,e,*], Shang Wang [b,*]

[a] Key Laboratory for Biomechanics and Mechanobiology of Ministry of Education, Beijing Advanced Innovation Center for Biomedical Engineering, School of Biological Science and Medical Engineering, School of Engineering Medicine, Beihang University, Beijing, 100191, China
[b] National Center for Neurological Disorders, Vascular Neurology, Department of Neurology, Beijing Tiantan Hospital, Capital Medical University, Beijing, 100070, China
[c] Department of Cardiology, The Cardiac Arrhythmia Center, State Key Laboratory of Cardiovascular Disease, National Clinical Research Center of Cardiovascular Diseases, Fuwai Hospital, National Center for Cardiovascular Diseases, Chines Academy of Medical Sciences and Peking Union Medical College, Beijing, 100037, China
[d] Vita Tech Innovation Center, Tsinghua Changgung Hospital, School of Clinical Medicine, Tsinghua University, Beijing, 100084, China
[e] School of Biomedical Engineering, Tsinghua University, Beijing, 100084, China
[f] Institute of Nanoenergy and Nanosystems, Chinese Academy of Sciences, Beijing, 101400, China
[g] China National Clinical Research Center for Neurological Diseases, Beijing, 100070, China

ARTICLE INFO

Keywords:
Cardiovascular diseases
Pacing lead
Blood pressure monitoring
Flexible electronics
Piezoelectric effect

ABSTRACT

Cardiac pacemakers are effective interventions for arrhythmias. However, conventional pacemakers lack the capability for real-time monitoring of hemodynamic parameters, which are crucial for diagnosing cardiovascular diseases and optimizing pacing parameters. Moreover, lead dislodgement, a common complication, can lead to serious consequences such as pacing failure. In this work, we developed a multi-functional passive fixation lead using force-electric conversion materials, enabling simultaneous continuous monitoring of intracardiac blood pressure and real-time evaluation of the lead's fixation status. In vitro and in vivo experiments demonstrated that the system allows for minimally invasive implantation, accurately captures blood pressure changes and can identify lead dislodgement. This study provides an integrated solution for precise diagnosis and treatment of cardiovascular diseases, offering significant potential for clinical application.

1. Introduction

Cardiovascular diseases (CVDs), one of the leading causes of death worldwide, constitutes a severe threat to patient health and survival, with a profound concomitant reduction in quality of life and a heavy medical and economic burden on families and society [1,2]. Among various types of CVDs, arrhythmia is one of the most common clinical manifestations [3]. Currently, the implantation of cardiac pacemakers represents the most effective treatment for arrhythmias [4,5]. By collecting the electrocardiographic (ECG) signals, cardiac pacemakers can accurately assess cardiac rhythm and use this information as a critical basis for pacing [6,7]. As a key component of the cardiac pacemaker system, pacing leads are responsible for transmitting electrical pulses from the pulse generator to the heart, and sensing or collecting the heart's electrical signals through electrodes. Currently, pacing leads commonly used in clinical practice can be classified into active fixation leads and passive fixation leads. Among them, passive fixation leads are widely adopted because of their reliable fixation and operational simplicity [8,9]. However, these leads are only capable of collecting ECG signals and cannot monitor hemodynamic parameters or cardiac mechanical function. For many CVDs, hemodynamic parameters are important monitoring indicators and diagnostic criteria [10]. In

* Corresponding authors.
** Correspondence to: Z. Liu, Key Laboratory for Biomechanics and Mechanobiology of the Ministry of Education, Beijing Advanced Innovation Center for Biomedical Engineering, School of Biological Science and Medical Engineering, School of Engineering Medicine, Beihang University, Beijing 100191, China.
E-mail addresses: liuzhuo@buaa.edu.cn (Z. Liu), li_zhou@tsinghua.edu.cn (Z. Li), drwangshang@foxmail.com (S. Wang).
[1] These authors contributed equally.

https://doi.org/10.1016/j.cej.2026.177655
Received 25 February 2026; Received in revised form 14 April 2026; Accepted 7 May 2026
Available online 24 May 2026
1385-8947/© 2026 Elsevier B.V. All rights are reserved, including those for text and data mining, AI training, and similar technologies.

particular, intracardiac blood pressure (BP) is a key physical parameter for assessing cardiac function, diagnosing various CVDs [11–13], and optimizing pacemaker parameter settings. Furthermore, lead dislodgement is one of the most common complications following pacemaker implantation [14]. Additionally, there is a lack of effective methods to monitor the fixation status of passive fixation leads. These issues significantly impact the therapeutic efficacy of pacemakers, potentially leading to increased pacing thresholds, poor sensing, or even pacing failure, which may necessitate surgical reintervention for lead repositioning in severe cases [15].

For various CVDs, a large body of research has focused on implantable sensors [16–25]. However, nearly all intracardiac sensors require thoracotomies to place the device directly inside the body. This invasive approach leads to a range of sequelae, thereby limiting its clinical translation. With technological advancements, cardiac pacemakers are evolving to be more intelligent and multifunctional [7,26,27]. Nevertheless, existing pacemakers remain primarily limited to ECG signal acquisition. Although cutting-edge studies have explored bioenergy harvesting and BP signal monitoring [28–32], most current implantable monitoring devices only possess a single sensing function: they can merely collect data on patients' physiological indicators, without enabling real-time therapeutic intervention when abnormalities are detected. In the implantation of related devices, traditional rigid medical implants are prone to induce device-related complications [33], while flexible implants have been widely adopted in the field of cardiovascular monitoring [34,35]. Among these, flexible piezoelectric materials have been extensively used in various implantable and interventional devices for collecting diverse human physiological signals [20,36–45], owing to their advantages of simple preparation, high energy conversion efficiency, and no requirement for an additional power supply [46–48]. Meanwhile, no suitable monitoring method currently exists for lead dislodgement, which is typically detected and addressed only after clinical symptoms manifest in patients. Therefore, to achieve timely intervention for CVDs and effectively improve disease treatment outcomes, the development of integrated devices that combine BP monitoring, lead fixation detection, and therapeutic functions have become a crucial direction in the development of current CVDs diagnosis and treatment technologies, and hold extremely significant clinical value.

In this work, we developed a multi-functional passive fixation lead (MPFL) for diagnosis and treatment of cardiac diseases based on flexible functional materials capable of force-electric conversion. While maintaining conventional pacing functions, this device enables monitoring of intracardiac BP. It can track BP changes within the cardiac chambers in real time with high precision and deliver timely synchronized electrical stimulation, thereby achieving simultaneous monitoring and therapeutic intervention. Simultaneously, the MPFL provides real-time feedback on post-implant fixation status, allowing prompt detection of lead dislodgement to ensure stable device operation and treatment efficacy. Furthermore, the entire sensing unit operates with zero power consumption. The MPFL mainly consists of two core functional units: The BP Monitoring Unit (BPMU), which is centered on a curl-fixed piezoelectric sensor. This unit can accurately capture BP changes in the right ventricle, and exhibits excellent linearity and stability, meeting the high-precision requirements for BP monitoring in clinical practice. The Fixation Monitoring Unit (FMU), which is based on arrayed sensors attached to a wing-like structure, by sensing the differences in sensor deformation caused by cardiac motion, this unit realizes real-time monitoring of the fixation status of the pacing lead. This system can be delivered via an interventional catheter, without the need for major invasive surgery, which effectively reduces surgical risks and patient suffering. To verify the effectiveness and reliability of this system, we conducted animal experiments. The experimental results showed that, in the bodies of large animals, the BP monitoring unit still maintained good linearity and could accurately reflect the changes in BP within the animals. Meanwhile, the position monitoring unit could generate signals with significant differences under different fixation conditions, which fully proves the feasibility of this unit for monitoring the position of pacing leads. This work provides a new technical paradigm for the development of next-generation full-function cardiac implantable electronic devices and is expected to make important contributions to advancing the treatment for CVDs and enhancing patient prognosis.

2. Results and discussions

2.1. The design and principle of MPFL

The MPFL comprises two main modules: BPMU for ventricular BP monitoring and FMU for assessing the fixation status of the pacemaker lead (Fig. 1a). The BPMU consists of a piezoelectric sensor (PS) with a length of 5 mm and a width of 3 mm, the PS is curled and secured onto the catheter wall of the pacing lead to detect variations in intraventricular BP. The FMU is designed as an array sensor comprising four PSs, each with a length of 4 mm and a width of 0.8 mm and each PS is mounted on the wing-like structure at the distal tip of the lead, with half of the PS located on the wing and the other half on the lead body. By monitoring the deformation of the wing-like structures induced by compression under different cardiac contraction states, the FMU reflects the fixation status of the lead. A photograph of the MPFL is shown in Fig. 1b. Each PS primarily comprises five layers (Fig. 1c and S1), including a poly(vinylidene fluoride) (PVDF)-based piezoelectric layer, silver electrodes, and thermoplastic polyurethane (TPU) encapsulation layers and all PSs were fabricated using the same procedure (Fig. S2).

The operating states of the MPFL after implantation into the ventricle under dislodgement and normal fixation conditions are shown in Fig. 1d. BPMU is positioned within the ventricle, where it experiences ventricular BP and transduces the pressure signal into electrical output. Under normal fixation conditions, cardiac contraction compresses the wing-like structure at the distal end of the pacing lead, inducing deformation of the attached FMU and thereby generating electrical signal. In contrast, when lead dislodgement occurs, the wing-like structure cannot be effectively anchored to the endocardium, and the FMU fails to produce a regular electrical output during cardiac contraction. Nevertheless, deformation of the PS elements may still occur due to ventricular blood flow, lead motion, and other disturbances, resulting in irregular electrical signals. Therefore, changes in the electrical output can be used to assess the fixation status of the pacing lead. The overall system workflow is shown in Fig. 1e. The sensing module acquires intracardiac BP signals and the fixation status of the pacing lead, and the collected signals are transmitted to the signal processing module. The signal processing module analyzes and processes the data and wirelessly transmits the results to an external device by Bluetooth. Once characteristic BP signals are identified, the therapy module is activated to transmit pacing pulses from the pulse generator to the heart via the pacing lead, thereby achieving real-time treatment. Meanwhile, the signals received by the external device can serve as clinical reference information, allowing patients to better understand their physiological status and enabling physicians to remotely monitor the data for further evaluation and diagnosis.

2.2. Working principle and electrical output performance of PS

The selection of materials and the fabrication process are closely associated with the final device performance. Among the flexible piezoelectric materials reported to date, PVDF exhibits excellent piezoelectric properties, however, its piezoelectric performance varies with film thickness. In this study, we customized three PVDF films with thicknesses of 110 μm, 56 μm, and 28 μm and performed their characterization. First, we measured the piezoelectric coefficient (d_{33}) of the three films. As shown in Fig. 2a, thicker PVDF films exhibited higher d_{33}. Subsequently, X-ray diffraction (XRD) revealed a pronounced characteristic peak at 20.7° for all three thicknesses, corresponding to the β

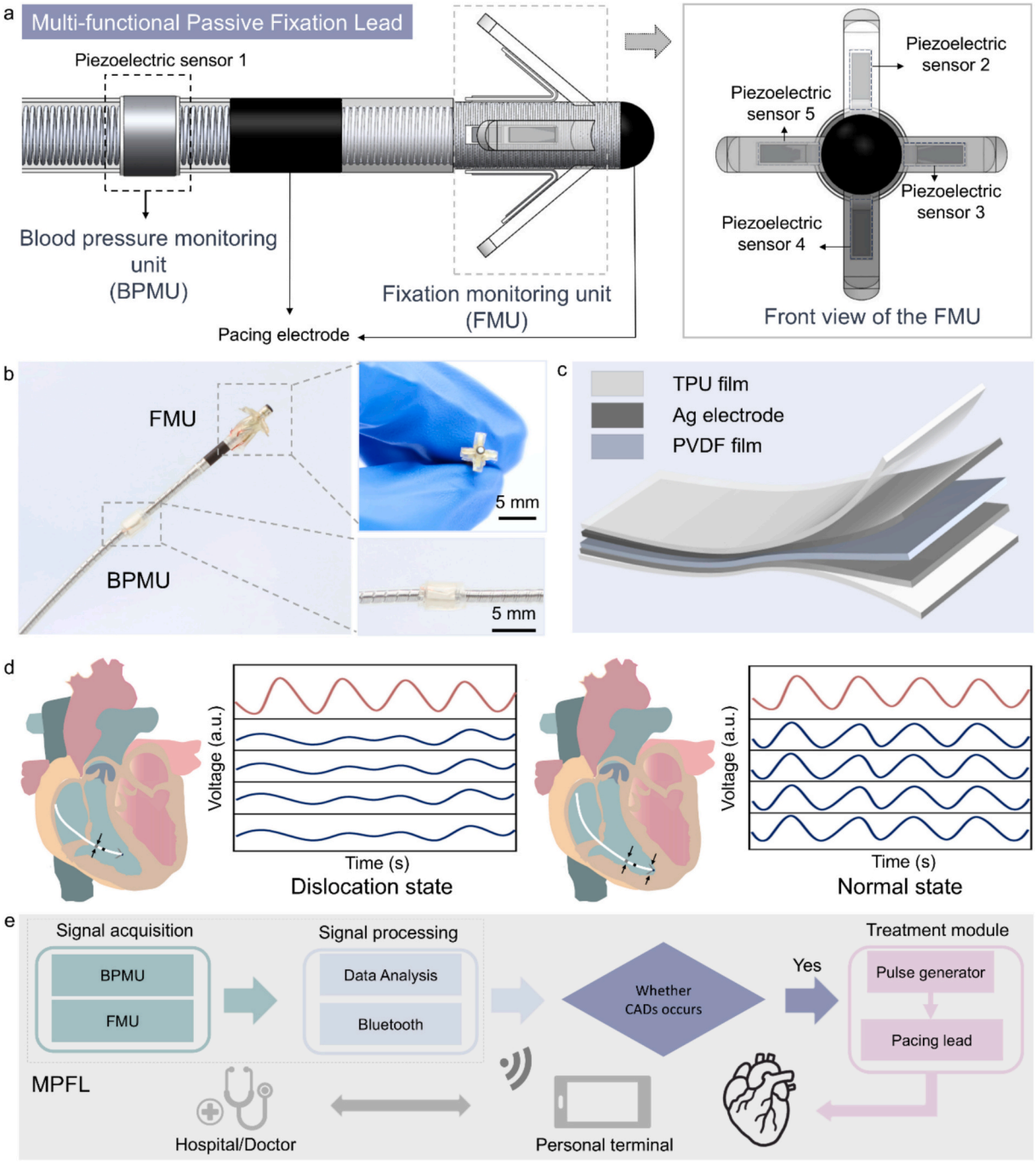

Fig. 1. The illustration and design of the MPFL. (a) Structural schematic of the MPFL. (b) Photograph of the MPFL. (c) Schematic of the PS structure. (d) Operating states and representative outputs of each module of the MPFL under normal fixation and dislodgement conditions. (e) Workflow of the MPFL system.

phase of PVDF, which provides the strongest piezoelectric response. Consistently, Fourier transform infrared (FT-IR) spectra showed characteristic bands at 1275 cm^{-1} and 839 cm^{-1}, which are also attributed to the β phase. The characteristic peaks were nearly identical across the different thicknesses, indicating no significant differences in structure or composition among the PVDF films (Fig. 2b, c).

During operation, the PS primarily subjected to two mechanical loading modes: compression and bending. The working principles under these two modes are illustrated in Fig. 2d, e. In the absence of external force, the internal dipoles remain in an equilibrium state. When the device is compressed by external mechanical motion, dipole rotation occurs, driving electrons to flow through the external circuit and generating an electrical current. Similarly, when the device is bent by an external force, dipole rotation is also induced, resulting in a certain amount of current output. For the electrical output under compressive loading, the piezoelectric response is primarily related to the applied force (F) and the d_{33}, and the open-circuit voltage (V_{OC}) can be expressed as (Note S1):

$$V_{OC} = \frac{d_{33} TF}{\varepsilon_0 \varepsilon_r A} \quad (1)$$

where T is the thickness of the piezoelectric material, ε_0 is the vacuum dielectric constant, ε_r is the relative dielectric constant of the piezoelectric material, and A is the area of the electrode of the piezoelectric element.

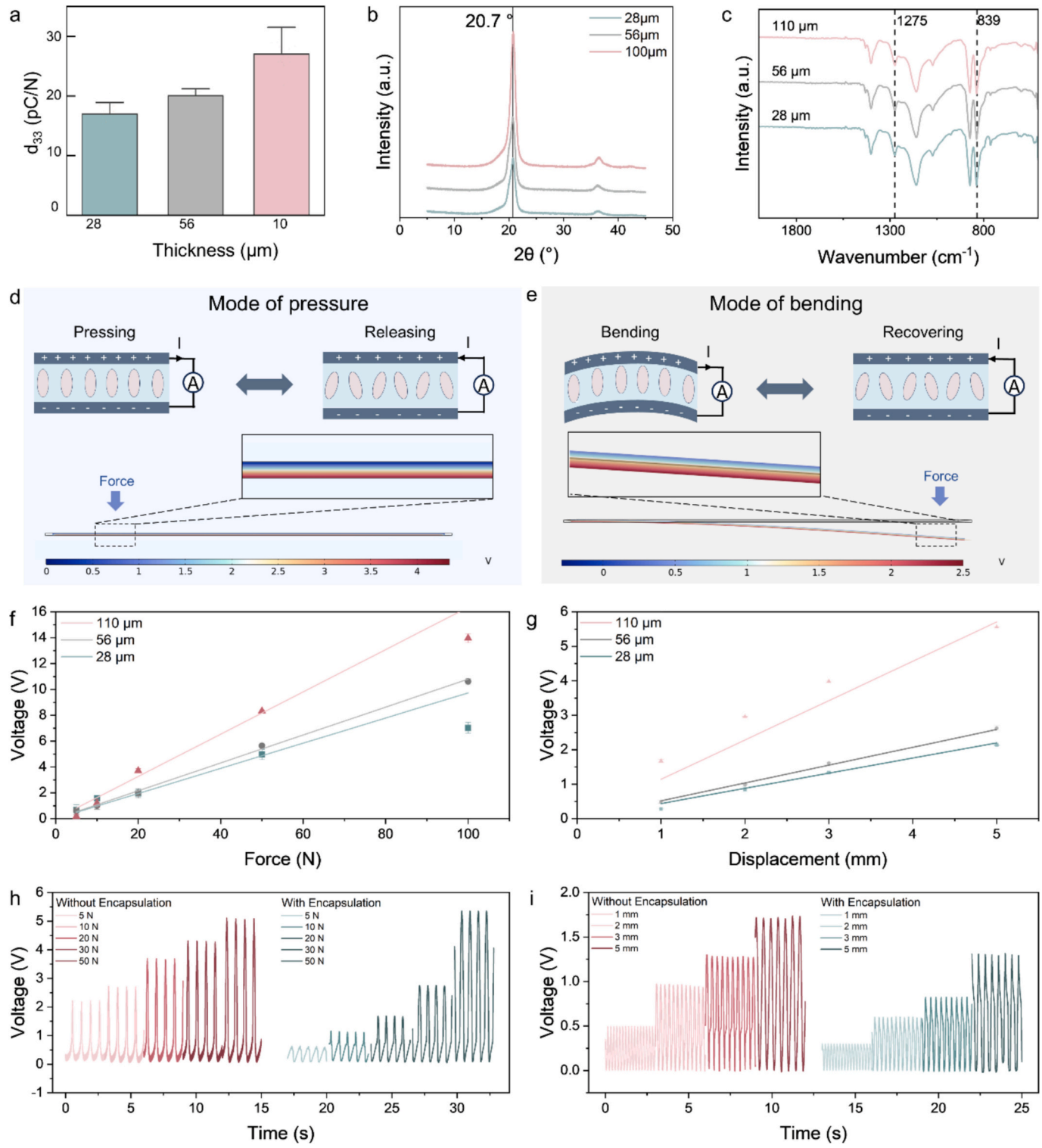

Fig. 2. Characterization of the material and PS. (a) d_{33} test of PVDF film with different thicknesses (28 μm, 56 μm and 110 μm). (b) XRD test of PVDF film with different thicknesses (28 μm, 56 μm and 110 μm). (c) FT-IR test of PVDF film with different thicknesses (28 μm, 56 μm and 110 μm). (d) Illustrations of the working principles of the PS under pressure mode. (e) Illustrations of the working principles of the PS under bending modes. (f) V_{OC} of PS fabricated with PVDF layers of different thicknesses under various pressures. (g) V_{OC} of PS fabricated with PVDF layers of different thicknesses under different bending conditions. (h) V_{OC} of PS under pressure conditions before and after packaging. (i) V_{OC} of PS under bending condition before and after packaging.

For the output under bending, the piezoelectric effect is mainly related to the deformation of the material in the thickness direction, specifically involving the piezoelectric constant d_{31}. Thus, the V_{OC} can be expressed as (Note S2) [49]:

$$V_{OC} = \frac{3d_{31}\pi kET^2}{2L^2\varepsilon_r}D \tag{2}$$

where L and T are the length and thickness of the cantilever beam, k is

Coulomb's constant, and E and ε_r represent the Young's modulus and the relative dielectric constant of the piezoelectric material, respectively. D is the displacement in the thickness direction.

To further characterize the performance differences among PVDF films with different thicknesses, we established a measurement setup to evaluate the V_{OC} of PSs fabricated from each thickness under both compressive loading and bending conditions. The output results under compression and bending are shown in Fig. 2f, g. Among the three thicknesses, the PS based on 110 μm PVDF film exhibited the highest sensitivity of 81.77 mV/N. In comparison, the sensitivities of the PSs based on 56 μm and 28 μm films were 53.96 mV/N and 48.68 mV/N, respectively, with only a slight difference observed between the latter two. Interestingly, as can be observed in Fig. 2d, under small applied forces, the PS fabricated from the 28 μm film showed the highest output, which may be attributed to the larger deformation induced under low-load conditions.

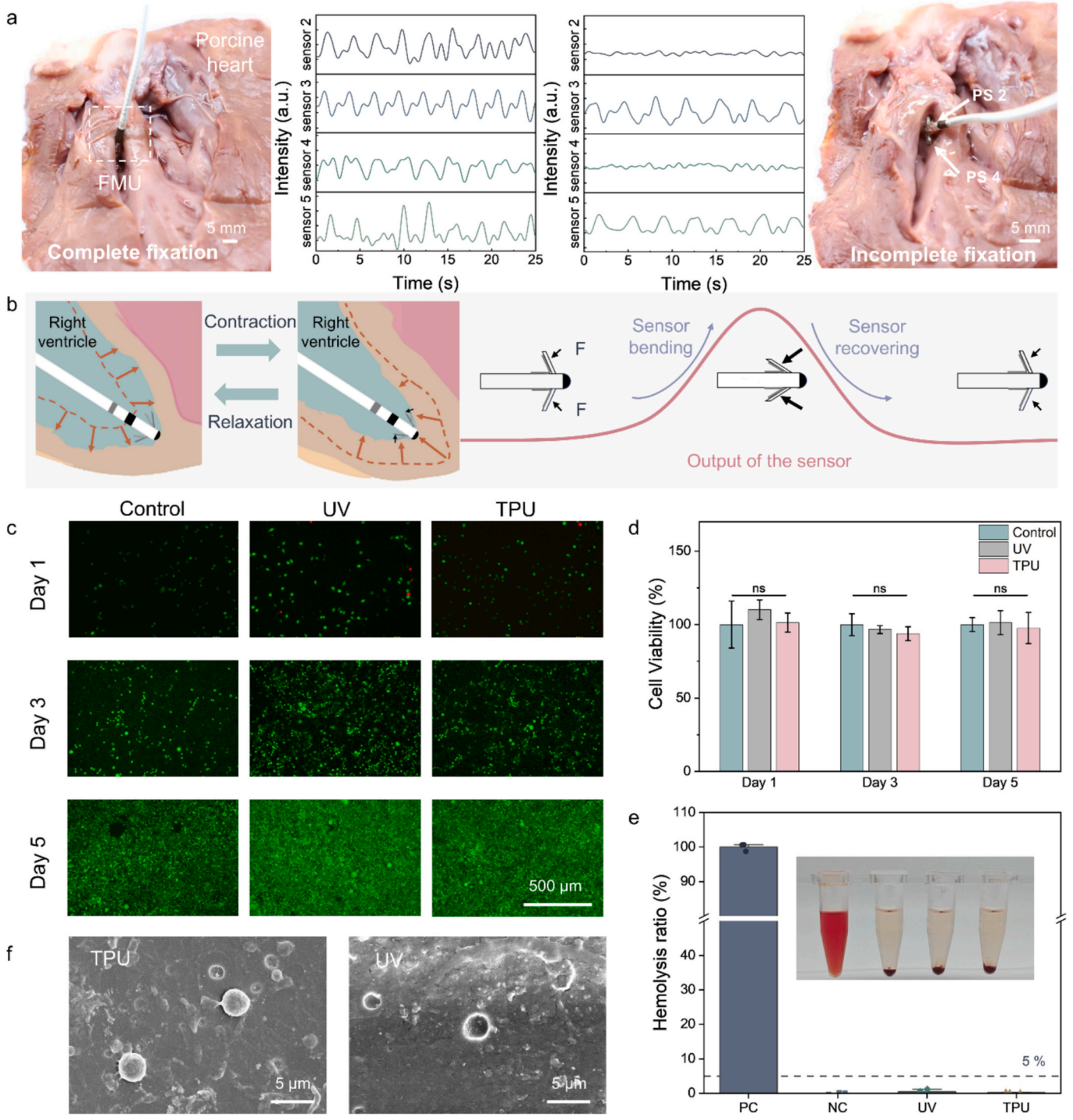

Fig. 3. In vitro characterization of the MPFL. (a) FMU output voltage under different fixation conditions. (b) Illustration of the FMU working principle. (c) Live/dead staining results of the control group, UV curable adhesive group and TPU group on day 1, day 3 and day 5. (d) Cells of the control group, UV curable adhesive group and TPU group on day 1, day 3 and day 5 absorbance result of CCK-8. ($n = 5$). (e) The hemolysis ratio of the UV curable adhesive group and the TPU group ($n = 3$). (f) SEM images of coagulation experiment in the UV curable adhesive group and the TPU group.

Although thicker films generally provided better electrical performance, PSs fabricated from thicker PVDF were mechanically stiffer, making it difficult to conform to the surface and the wing-like structures of the pacing lead. Moreover, under in vivo conditions, the force applied to the PS is limited, and it is challenging to induce appreciable deformation in thicker PVDF. The deflection of the material based on a cantilever-beam model can be expressed as:

$$\delta_{max} = \frac{4FL^3(1-\nu^2)}{Ebh^3} \quad (3)$$

where L and h are the length and thickness of the cantilever beam, b represents the width of the material, E is Young's modulus, and ν is the Poisson's ratio of the material.

According to the equation, under the same applied force the deformation of the material is inversely proportional to the cube of its thickness; thus, thinner films undergo larger deformation. Therefore, the PVDF film with a thickness of 28 μm was ultimately selected as the sensing material.

In addition, the influence of the encapsulation layer on PS performance was investigated by measuring the electrical outputs of the PS before and after encapsulation (Fig. 2h, i). Under both pressure and bending conditions, the performance of the encapsulated PS decreased to 56.74% and 65.59% of its original output. This reduction was attributed to the encapsulation layer, which partially restricted the deformation of the PS, leading to a decrease in its output.

2.3. In vitro evaluation of the MPFL

We separately evaluated the BPMU and FMU in vitro to verify the feasibility of each module. The FMU was tested using an ex vivo porcine heart. By altering the fixation conditions of the wing-like structures, we assessed its capability to monitor lead fixation (Fig. S3). As shown in Fig. 3a, under complete fixation with all four wings securely anchored, each PS generated regular electrical output. In contrast, when only the two contralateral wings were fixed, the PSs lacking effective anchoring produced little to no measurable signal. These results indicate that the FMU output differs markedly under different fixation states. Fig. 3b illustrates the working principle after implantation in the right ventricle. Under normal fixation, the PS elements within the FMU undergo periodic bending synchronized with cardiac systole and diastole, generating regular electrical signals, whereas unfixed PS elements experience minimal deformation and therefore produce no detectable electrical output, allowing effective monitoring of the fixation state. Meanwhile, the BPMU was characterized by measuring the output voltage of the PBMU under gradient force conditions (Fig. S4). Subsequently, a simulated fluid pressure test was conducted using a circulating pump system to mimic liquid pressure variations (Fig. S5). Pressure conditions were modulated by adjusting parameters such as the pump flow rate, and calibration was performed using a commercial signal monitoring instrument. The fitting results in Fig. S6 indicate that the BPMU achieves a sensitivity of 1.63 mV/mmHg in a liquid environment, demonstrating its excellent performance. To verify the stability of the sensor during long-term implantation, the sensor was immersed in phosphate-buffered saline (PBS) to simulate the physiological fluid environment, and a fatigue test of 1,000,000 cycles was conducted. The variation in device output with increasing cycle number was evaluated at a frequency of 2 Hz, and the output performance of the sensor was measured every 200,000 cycles. The results showed that, after 1,000,000 cycles, the sensor output remains at 93.6% of that before the fatigue test, and the sensor performance remains stable (Fig. S7). In addition, the cross-sections of the sensor before and after the fatigue test were characterized using a metallographic microscope (Fig. S8). The images showed that no separation occurred in the TPU encapsulation layer after the fatigue test, and the overall sensor structure remained stable.

In addition, biocompatibility is essential for implantable electronic devices. Prior to animal experiments, we conducted a comprehensive biocompatibility assessment of the encapsulation material (TPU) and the UV curable adhesive used for fixation. Regarding cytocompatibility, live/dead staining revealed no apparent differences between the TPU and UV curable adhesive groups and the control group (Fig. 3c). The CCK-8 assay further confirmed the favorable cytocompatibility of both materials (Fig. 3d). Since the device is intended to reside in a blood environment for extended periods, evaluation of hemocompatibility is a critical prerequisite for safe in vivo application. We evaluated the blood compatibility of positive control (water), negative control (phosphate buffered saline), and two materials using hemolysis experiments. The results showed pronounced hemolysis in the positive control group, whereas the hemolysis rates of the TPU and UV curable adhesive groups were well below the 5% threshold specified in ISO 10993–4:2002 (Fig. 3e). Moreover, scanning electron microscopy (SEM) images of platelet adhesion on the encapsulation layer indicated that platelets maintained a rounded morphology without aggregation (Fig. 3f).

2.4. In vivo monitoring of MPFL

To evaluate the effectiveness of the MPFL for in vivo monitoring, a large-animal study was conducted using a beagle dog. Following implantation of the MPFL into the canine heart, signals from the BPMU and FMU were analyzed (Fig. 4a). In parallel, a data acquisition hardware (MP150 BIOPAC System, INC.) was used to measure heart rate and BP as reference data. The MPFL was delivered and implanted via an introducer sheath (Fig. 4b). The sensors included PS 1 in the BPMU and PS 2 to PS 5 in the FMU. After successful implantation, real-time signals from all sensors were acquired (Fig. 4c). After implantation of the MPFL, the heart rate, blood pressure, and other parameters of the beagle dogs remained stable and within normal ranges, with no impact on the animals' normal physiological functions. Notably, the electrical signal variation measured by PS 1 was nearly perfectly synchronized with the BP waveform recorded by the MP150, demonstrating the feasibility of this module as a BP sensor. Further analysis of the BPMU signal revealed that, in addition to a prominent main peak, smaller peaks were also present. These subtle fluctuations correspond to different cardiac activity states. For example, the fluctuation at position I in Fig. 4d represents atrial contraction, reflecting pressure changes caused by blood inflow into the ventricle. We also observed a clear segmentation in the slope during the rising phase of the signal, which corresponds to the isovolumetric contraction and rapid ejection phases of ventricular systole. These fine-scale variations indicate that the BPMU possesses high sensitivity and can effectively distinguish different phases of cardiac motion.

Meanwhile, the FMU generated regular electrical signals synchronized with cardiac motion, with signal variations consistent with changes in heart rate and maintaining stable performance. These results indicate that, under normal fixation, all FMU PSs produce periodic outputs driven by cardiac activity as expected. In addition, the basic pacing function of the MPFL was examined by pacing the animals at rest using a temporary pacemaker connected to the lead (Fig. 4e). A marked change in heart rate before and after pacing was observed, indicating that the added functional modules did not compromise the fundamental pacing performance. The pressure-monitoring capability of the BPMU was further investigated by administering a vasopressor and recording signal variations before and after drug intervention. After intervention, the signal measured by PS 1 increased synchronously with BP (Fig. S9). Quantitative evaluation of the monitoring performance was performed by comparing BP and heart rate signals recorded by the MP150 and the MPFL before and after pacing and drug intervention. First, heart rate signals recorded by the MP150 system were processed and compared with the electrical signals from the FMU. Heart rate tracking showed high consistency, with the two signals remaining nearly synchronized before and after pacing and drug intervention (Fig. 4f and S10). Subsequently, the sensitivity of the BPMU was characterized by quantifying

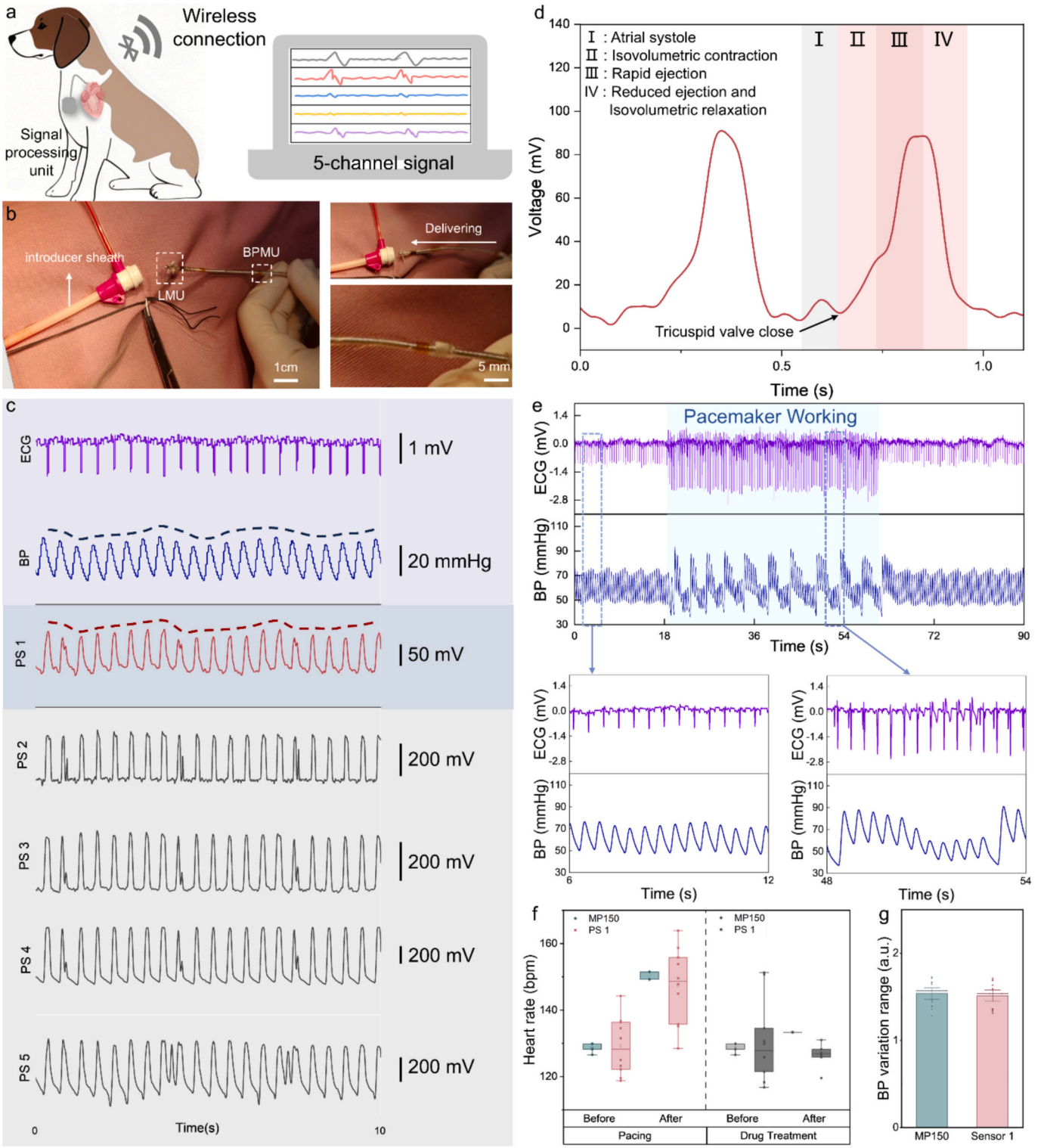

Fig. 4. In vivo characterization of the MPFL. (a) Schematic of signal acquisition and transmission in the animal experiment. (b) Photograph of MPFL implantation. (c) Signals recorded from each sensor after MPFL implantation, together with simultaneously acquired ECG and BP. (d) Analysis of the BP waveform measured by the BPMU. (e) ECG and BP recorded during pacing with a temporary pacemaker after MPFL implantation. (f) Heart rate statistics obtained from the signals recorded by Sensor 1 and MP150 simultaneously before and after different interventions(n = 40). (g) The variation range of BP signals recorded by Sensor 1 and MP150 simultaneously before and after drug intervention (n = 13).

the relative changes in blood pressure amplitude measured by the MP150 and BPMU before and after drug intervention (Fig. 4g). The two exhibited essentially consistent variation magnitudes, suggesting that the BPMU responds to pressure changes with good sensitivity and linearity, thereby demonstrating excellent monitoring capability.

To enable wireless transmission of the monitoring signals, we designed and tested a Wireless transmission unit, the working setup and the wireless module are shown in Fig. 5a. The animals were first subjected to cardiac pacing (Fig. 5b). PS 1 exhibited a pronounced voltage change before and after pacing, consistent with the pacing-induced BP

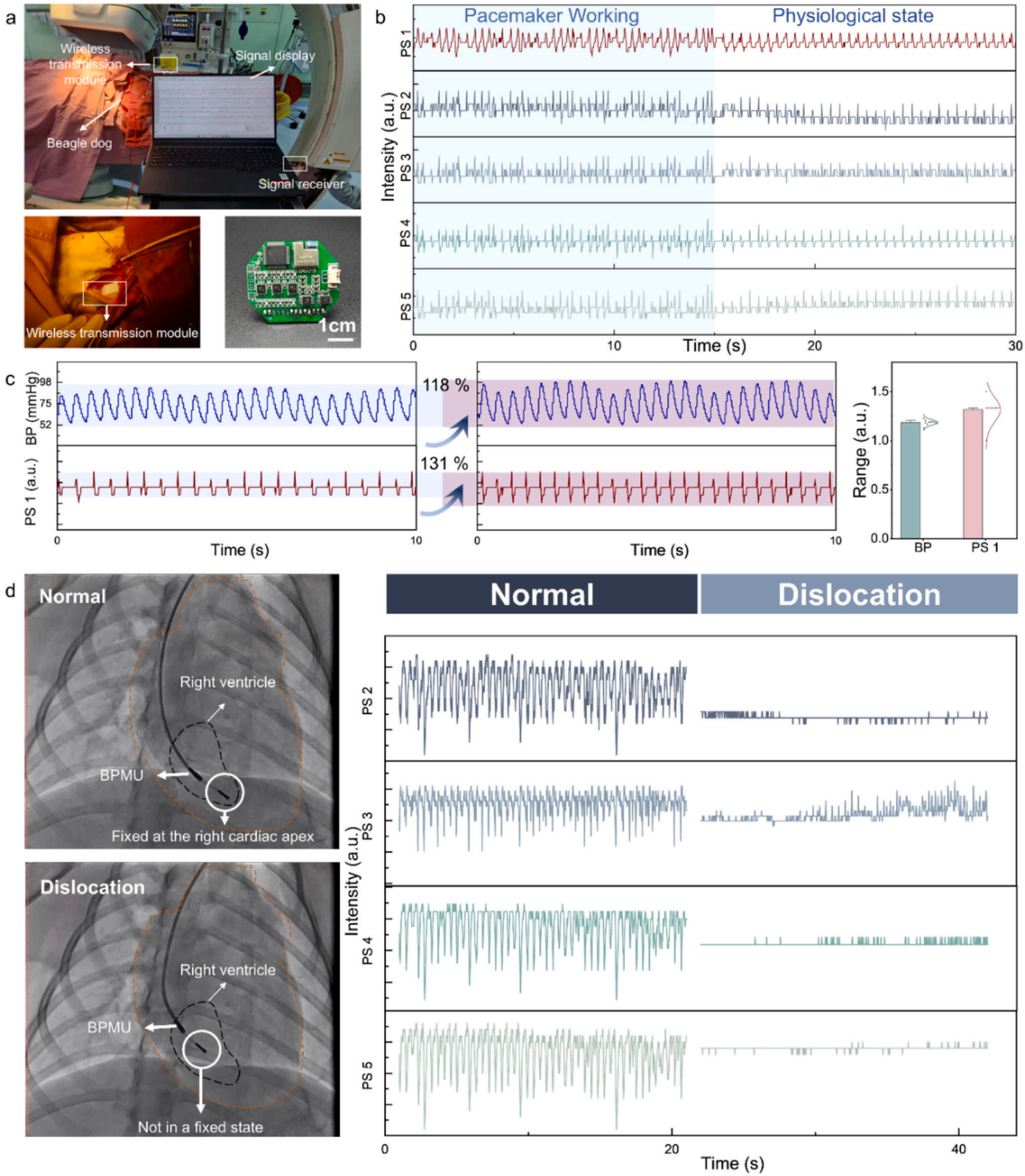

Fig. 5. Functional verification of MPFL implanted in animals. (a) Signal acquisition process after implantation. (b) Signals recorded from each sensor after implantation of the MPFL. (c) Comparison of the output signals of Sensor1 and MP150 before and after BP changes. (d) Signals from each sensor within the FMU under normal fixation and dislodgement states, along with the corresponding medical images.

variation, the other PSs also showed evident changes in signal amplitude. Subsequently, a vasopressor was administered to elevate BP. As shown in Fig. 5c, the BP signal from PS 1 increased synchronously with BP, and the magnitude of the increase was largely comparable, increased to 118% and 131% of the original values. These results are consistent with those obtained without the Bluetooth module, thereby validating the accuracy and effectiveness of the Bluetooth-based wireless unit.

Furthermore, we examined the signal differences of the FMU under different fixation states by retracting the entire lead after implantation to artificially induce electrode dislodgement. The fixation state was confirmed by imaging, and the FMU outputs were recorded (Fig. 5d). Imaging clearly shows that the FMU, indicated by the white circle, has detached from its normal fixation state and is floating within the ventricle. When lead dislodgement occurred, the FMU output signals

changed markedly. Under normal fixation, each sensor generated regular signals. After dislocation, only irregular signals or no detectable output were observed. This behavior can be attributed to the loss of periodic mechanical forces associated with cardiac contraction, as the displaced PSs were mainly influenced by blood pressure and irregular swinging motions, resulting in non-periodic electrical outputs. Notably, PS 3 exhibited large fluctuations, which may be attributable to swinging within the cardiac chamber and possible collisions with the ventricular wall (Fig. S11). These differences indicate that the FMU can effectively monitor the fixation status of the pacemaker lead and serve as a reliable indicator of lead dislodgement.

3. Conclusion

To address the clinical challenges in CVDs management, particularly the lack of real-time monitoring of intracardiac BP and lead fixation status, as well as the absence of immediate intervention capabilities, this study designs the MPFL to enable real-time intracardiac BP monitoring and pacing lead fixation tracking, thereby providing an innovative solution for precision management of CVDs. The device design achieves a balance between functional integration and minimally invasive architecture. Based on passive pacing lead, two core units, the BPMU and the FMU, are constructed by integrating PSs. These units are used to monitor intracardiac BP and accurately identify lead fixation status by leveraging deformation differences induced by cardiac motion. This approach preserves the minimally invasive characteristics of conventional pacing leads while adding the capability to monitor key physiological parameters, overcoming the limitation of existing pacemakers that collect only rhythm-related signals. The clinical potential of the device has been validated through both in vitro and in vivo experiments. The device addresses the limitations of conventional BP monitoring while simultaneously enabling timely intervention through electrical stimulation. Furthermore, its precise monitoring capability for intracardiac BP offers a potential tool for auxiliary diagnosis of CVDs such as heart failure, pulmonary hypertension, and orthostatic hypotension. Future work will focus on optimizing the backend system, utilizing deep learning and other methods to accurately identify characteristic pressure signals, achieve synchronous therapy upon monitoring, and form an integrated diagnostic-therapeutic closed loop, thereby proposing a novel solution for the next generation of intelligent healthcare.

4. Methods

4.1. Materials

The thermoplastic polyurethane (TPU) particles were purchased from Dongguan Jinheng Plastic Company Limited, *N*,*N*-dimethylformamide was obtained from Aladdin. The UV-curable glue was purchased from LOCTITE. The PBS buffer solution, DMEM high-glucose medium, CCK8 kit, paraformaldehyde, AM/PI kit used in the cell experiments were all purchased from Sorelbo. Fetal bovine serum was purchased from GIBCO.

4.2. Fabrication of MPFL

First, the customized polyvinylidene fluoride (PVDF) film with predeposited electrodes was cut into the desired dimensions. Second, lead wires were connected to the electrode layers on both sides of the PVDF film. Third, the piezoelectric sensor (PS) was encapsulated using thermoplastic polyurethane (TPU). Specifically, TPU pellets and *N*,*N*-dimethylacetamide were mixed at a mass ratio of 2:8 and continuously stirred under heating at 40 °C for 24 h to obtain a homogeneous solution. The resulting solution was then uniformly coated onto both sides of the piezoelectric sensor, and the encapsulated device was subsequently dried in an oven at 35 °C for 12 h. After the preparation of the PS, biological glue is used as the fixing medium to firmly install the sensor at the front end of the cardiac pacing lead and on the surface of the lead body respectively. Specifically, for the FMU, four sensors are respectively fixed on the four wing-shaped structures at the front end of the pacing lead. During the fixing operation, each sensor adopts a cross-regional bonding method, so that half of its area is firmly pasted on the surface of the wing-shaped structure, and the other half is attached to the body of the pacing lead. For the BPMU, according to the arc-shaped outer shape of the pacing lead body, the sensor is moderately bent and shaped, and then it is fixed on the lead body.

4.3. Characterization methods

The scanning electron microscopy (SEM) images were taken by a emission scanning electron microscope (SU 8020, Hitachi, Japan). The crystalline structure of the PVDF film was characterized using X-ray diffraction (X'Pert3, PANalytical, Poland). The d_{33} of the PVDF film was measured by a piezoelectric tester (ZJ-3 A, JKZC, China). The V_{OC} was detected by an electrometer (6517, Keithley, USA) and recorded by an oscilloscope (HDO6104, LeCroy, USA). For evaluation of the force–electrical output relationship, a push–pull dynamometer (Mark-10, USA) was used to quantitatively apply forces of varying magnitudes to the PS, while the V_{OC} of the device was simultaneously measured.

4.4. Cell compatibility testing

For the purpose of evaluating cell biocompatibility, leachates were separately prepared from the TPU film and UV curable adhesive. Specifically, 100 mg of each sterilized material was incubated in 50 mL of standard Dulbecco's Modified Eagle Medium (DMEM) at 37 °C for 48 h to obtain the corresponding leaching solutions. Subsequently, L929 cells were employed as the model cell line to carry out the cell biocompatibility assay. The cells were seeded in a 96-well plate, with the two leachate mediums as experimental groups and original DMEM as the control group. Cells were cultured at 37 °C with 95% air and 5% CO_2 for 1, 3, and 5 days. Live/dead staining was used to assess cell morphology and vitality. After fluorescent staining on days 1, 3, and 5, cell images were observed under a fluorescence microscope (DM6000, Leica, USA) at 490 ± 10 nm and 545 nm. To quantify cell viability, 10% CCK-8 solution was used, and cells were incubated for 2 h after washing three times with 1 × PBS. The absorbance at 450 nm was measured using a microplate reader (Varioskan Lux, Thermo Fisher, USA).

4.5. Hemocompatibility evaluation

Hemolysis and coagulation tests were performed for hemocompatibility evaluation. For the hemolysis test, 1 mL fresh rat blood was taken into an anticoagulant tube, and 2 mL PBS was added, then centrifuged at 1000 r for 5 min. The centrifugation was repeated four times until the supernatant became clear, after which the supernatant was discarded. The red blood cells were resuspended in 10 mL PBS as the blood working solution. In the experimental group, 200 μL of the blood working solution was mixed with 800 μL of material leachate (1 mg TPU film/ UV curable adhesive was immersed in 1 mL of PBS for 3 days), with an equal amount of blood working solution and water as the positive control (PC) and an equal amount of blood working solution and PBS as the negative control (NC). After incubating at 37 °C for 4 h, each sample was centrifuged at 1000 r for 5 min, and 100 μL of the supernatant was tested for absorbance at 577 nm. For the coagulation test, fresh blood from male 6-week-old SD rats (220 g) was taken (2 mL) and placed in a centrifuge tube for 30 min. The cells were centrifuged at 800 rpm for 10 min. Platelets were placed on sterile material (TPU and UV curable adhesive) and incubated at 37 °C for 90 min. After fixation with 4% paraformaldehyde (Solarbio, P1110) for 30 min, the samples were dehydrated in different concentrations of ethanol (25%, 50%, 60%, 70%, 80%, 90%, 95%, 100%) for 30 min. After drying at room temperature, platelet morphology on the scaffold surface was observed

using scanning electron microscopy.

4.6. Animal experiments

All experimental processes were strictly in line with the institutional and national guidelines for the care and use of laboratory animals and the study protocol was reviewed and approved by the Institutional Animal Care and Use Committee (IACUC), Fuwai Hospital, Chinese Academy of Medical Sciences (0108-3-15-ZX(X) – 22). Beagles were anesthetized with propofol (0.5 mg/kg), intubated and maintained on 1%–3% isoflurane with positive pressure ventilation. The left external jugular vein was routinely exposed. A short 8F sheath (HLS-1008 M; Medtronic) was advanced over a guidewire to obtain the access for lead implantation. Then the lead was inserted into the vein and was located in the right ventricular apex. To investigate the intra-cardiac pressure monitored by the lead, a moderate dose of dopamine (a kind of positive inotropic agent) was injected into the beagle vein to enhance cardiac contractility. Finally, beagles were euthanized for anatomical analysis. The animals were killed by injection of medium with high potassium concentration, and then the chest was opened to remove the heart.

CRediT authorship contribution statement

Xuandi Deng: Writing – original draft, Validation, Methodology, Investigation. **Yiran Hu:** Writing – original draft, Validation, Methodology, Investigation. **Puqing Yao:** Writing – original draft, Validation, Methodology, Investigation. **Chunhong Yu:** Investigation. **Juwei Yang:** Investigation. **Ruizeng Luo:** Investigation. **Sijing Cheng:** Investigation. **Hao Huang:** Investigation. **Peng Cheng:** Investigation. **Lei Jia:** Investigation. **Xingyao Lv:** Investigation. **Menghan Li:** Investigation. **Zetao Zhao:** Investigation. **Wei Hua:** Project administration. **Yongjun Wang:** Project administration. **Zhuo Liu:** Writing – review & editing, Project administration, Funding acquisition, Conceptualization. **Zhou Li:** Writing – review & editing, Project administration, Funding acquisition. **Shang Wang:** Writing – review & editing, Project administration, Funding acquisition.

Declaration of competing interest

The authors declare that they have no known competing financial interests or personal relationships that could have appeared to influence the work reported in this paper.

Acknowledgments

The authors thank the support of Beijing Nova Program (20250484871), National Natural Science Foundation of China (82372141, T2125003, U25A20417), Study on the Key Mechanisms, R&D and Application of Monitoring and Treatment Devices for Orthostatic Hypotension of Beijing Tiantan Hospital (2-3-1-543-01), Beijing Natural Science Foundation (Z240022, L245015, 25JL006), Scientific and Technological Innovation Project of China Academy of Chinese Medical Sciences (CI2023C020YL), Fundamental Research Funds for the General Universities.

Appendix A. Supplementary data

Supplementary data to this article can be found online at https://doi.org/10.1016/j.cej.2026.177655.

Data availability

Data will be made available on request.

References

[1] M. Naghavi, K. Ong, A. Aali, et al., Global burden of 288 causes of death and life expectancy decomposition in 204 countries and territories and 811 subnational locations, 1990-2021: a systematic analysis for the global burden of disease study 2021, Lancet 403 (2024) 2100–2132, https://doi.org/10.1016/s0140-6736(24)00367-2.
[2] G. Mensah, G. Roth, V. Fuster, The global burden of cardiovascular diseases and risk factors 2020 and beyond, J. Am. Coll. Cardiol. 74 (2019) 2529–2532, https://doi.org/10.1016/j.jacc.2019.10.009.
[3] M. Patel, S. Sampath, A. Kapoor, et al., Advances in cardiac pacing: arrhythmia prediction, prevention and control strategies, Front. Physiol. 12 (2021) 13, https://doi.org/10.3389/fphys.2021.783241.
[4] M. Brignole, A. Auricchio, G. Baron-Esquivias, et al., 2013 ESC guidelines on cardiac pacing and cardiac resynchronization therapy, Europace 15 (2013) 1070–1118, https://doi.org/10.1093/europace/eut206.
[5] S. Al-Khatib, Cardiac implantable electronic devices, N. Engl. J. Med. 390 (2024) 442–454, https://doi.org/10.1056/NEJMra2308353.
[6] J. Deng, X. Sun, H. Peng, Power supplies for cardiovascular implantable electronic devices, EcoMat 5 (2023) 15, https://doi.org/10.1002/eom2.12343.
[7] E. Cingolani, J. Goldhaber, E. Marbán, Next-generation pacemakers: from small devices to biological pacemakers, Nat. Rev. Cardiol. 15 (2018) 139–150, https://doi.org/10.1038/nrcardio.2017.165.
[8] L. Liu, J. Tang, H. Peng, et al., A long-term, prospective, cohort study on the performance of right ventricular pacing leads: comparison of active-fixation with passive-fixation leads, Sci. Rep. 5 (2015), https://doi.org/10.1038/srep07662.
[9] W. DeForge, Cardiac pacemakers: a basic review of the history and current technology, J. Vet. Cardiol. 22 (2019) 40–50, https://doi.org/10.1016/j.jvc.2019.01.001.
[10] P. Blankestijn, M. Bots, Device therapy for uncontrolled hypertension: new approaches to an old problem, Nat. Rev. Nephrol. 13 (2017) 725–726, https://doi.org/10.1038/nrneph.2017.150.
[11] S. Robinson, L. Ring, D. Oxborough, et al., The assessment of left ventricular diastolic function: guidance and recommendations from the British Society of Echocardiography, Echo Res. Pract. 11 (2024) 55, https://doi.org/10.1186/s44156-024-00051-2.
[12] T. McDonagh, M. Metra, M. Adamo, et al., ESC guidelines for the diagnosis and treatment of acute and chronic heart failure, Eur. Heart J. 42 (2021) (2021) 3599–3726, https://doi.org/10.1093/eurheartj/ehab368.
[13] G. Simonneau, D. Montani, D. Celermajer, et al., Haemodynamic definitions and updated clinical classification of pulmonary hypertension, Eur. Respir. J. 53 (2019) 13, https://doi.org/10.1183/13993003.01913-2018.
[14] Y. Wang, W. Hou, C. Zhou, et al., Meta-analysis of the incidence of lead dislodgement with conventional and leadless pacemaker systems, PACE-Pacing Clin. Electrophysiol. 41 (2018) 1365–1371, https://doi.org/10.1111/pace.13458.
[15] M. Braun, T. Rauwolf, M. Bock, et al., Percutaneous lead implantation connected to an external device in stimulation-dependent patients with systemic infection - a prospective and controlled study, Pacing Clin. Electrophysiol. 29 (2006) 875–879, https://doi.org/10.1111/j.1540-8159.2006.00454.x.
[16] N. Oyunbaatar, J. Wei, L. Wang, et al., 3D-printed CNT-reinforced bioresorbable vascular scaffold with enhanced mechanical stability and integrated wireless pressure sensor for continuous hemodynamic monitoring, ACS Sens. 10 (2025) 5724–5735, https://doi.org/10.1021/acssensors.5c00857.
[17] Z. Cao, Y. Liu, B. Sun, et al., A high-stability pressure-sensitive implantable memristor for pulmonary hypertension monitoring, Adv. Mater. 37 (2025) 12, https://doi.org/10.1002/adma.202411659.
[18] X. Qu, S. Cheng, Y. Liu, et al., Bias-free cardiac monitoring capsule, Adv. Mater. 36 (2024), https://doi.org/10.1002/adma.202402457.
[19] R. Omar, W. Saliba, M. Khatib, et al., Biodegradable, biocompatible, and implantable multifunctional sensing platform for cardiac monitoring, ACS Sens. 9 (2024) 126–138, https://doi.org/10.1021/acssensors.3c01755.
[20] C. Wang, Y. Hu, Y. Liu, et al., Tissue-adhesive piezoelectric soft sensor for in vivo blood pressure monitoring during surgical operation, Adv. Funct. Mater. 33 (2023) 10, https://doi.org/10.1002/adfm.202303696.
[21] K. Kwon, J. Kim, S. Won, et al., A battery-less wireless implant for the continuous monitoring of vascular pressure, flow rate and temperature, Nat. Biomed. Eng. 7 (2023) 1215–1228, https://doi.org/10.1038/s41551-023-01022-4.
[22] C. Boutry, L. Beker, Y. Kaizawa, et al., Biodegradable and flexible arterial-pulse sensor for the wireless monitoring of blood flow, Nat. Biomed. Eng. 3 (2019) 47–57, https://doi.org/10.1038/s41551-018-0336-5.
[23] T. Li, Z. Feng, M. Qu, et al., Core/shell piezoelectric nanofibers with spatial self-orientated β-phase nanocrystals for real-time micropressure monitoring of cardiovascular walls, ACS Nano 13 (2019) 10062–10073, https://doi.org/10.1021/acsnano.9b02483.
[24] Z. Ma, J. Zhang, S. Zou, et al., Smart vascular grafts with integrated flow biosensors for hemodynamic real-time monitoring and vascular healthcare, ACS Nano 19 (2025) 7661–7676, https://doi.org/10.1021/acsnano.4c09980.
[25] J.W. Nam, C.H. Moon, D.H. Kim, et al., Dynamically crosslinked poly(vinyl alcohol)/borax strain sensors for organ motion monitoring, Chem. Eng. J. 498 (2024) 10, https://doi.org/10.1016/j.cej.2024.155748.
[26] D. Keene, A. Arnold, M. Jastrzebski, et al., His bundle pacing, learning curve, procedure characteristics, safety, and feasibility: insights from a large international observational study, J. Cardiovasc. Electrophysiol. 30 (2019) 1984–1993, https://doi.org/10.1111/jce.14064.

[27] P. Defaye, M. Biffi, M. El-Chami, et al., Cardiac pacing and lead devices management: 25 years of research at EP Europace journal, Europace 25 (2023) 16, https://doi.org/10.1093/europace/euad202.
[28] L. Dong, C. Wen, Y. Liu, et al., Piezoelectric buckled beam array on a pacemaker lead for energy harvesting, Adv. Mater. Technol. 4 (2019) 9, https://doi.org/10.1002/admt.201800335.
[29] N. Li, Z. Yi, Y. Ma, et al., Direct powering a real cardiac pacemaker by natural energy of a heartbeat, ACS Nano 13 (2019) 2822–2830, https://doi.org/10.1021/acsnano.8b08567.
[30] H. Ouyang, Z. Liu, N. Li, et al., Symbiotic cardiac pacemaker, Nat. Commun. 10 (2019) 10, https://doi.org/10.1038/s41467-019-09851-1.
[31] L. Dong, A. Closson, C. Jin, et al., Multifunctional pacemaker lead for cardiac energy harvesting and pressure sensing, Adv. Healthc. Mater. 9 (2020) 12, https://doi.org/10.1002/adhm.202000053.
[32] Z. Liu, Y. Hu, X. Qu, et al., A self-powered intracardiac pacemaker in swine model, Nat. Commun. 15 (2024) 11, https://doi.org/10.1038/s41467-023-44510-6.
[33] X. Fan, L. Zhu, K. Wang, et al., Stiffness-controlled thermoresponsive hydrogels for cell harvesting with sustained mechanical memory, Adv. Healthc. Mater. 6 (2017) 10, https://doi.org/10.1002/adhm.201601152.
[34] Y. Hong, H. Jeong, K. Cho, et al., Wearable and implantable devices for cardiovascular healthcare: from monitoring to therapy based on flexible and stretchable electronics, Adv. Funct. Mater. 29 (2019) 26, https://doi.org/10.1002/adfm.201808247.
[35] T. Truong, X. Huang, M. Barton, et al., Flexible electrode arrays based on a wide bandgap semiconductors for chronic implantable multiplexed sensing and heart pacemakers, ACS Nano 19 (2025) 1642–1659, https://doi.org/10.1021/acsnano.4c15294.
[36] G. Hwang, M. Byun, C. Jeong, et al., Flexible piezoelectric thin-film energy harvesters and nanosensors for biomedical applications, Adv. Healthc. Mater. 4 (2015) 646–658, https://doi.org/10.1002/adhm.201400642.
[37] A. Al-Qatatsheh, Y. Morsi, A. Zavabeti, et al., Blood pressure sensors: materials, fabrication methods, performance evaluations and future perspectives, Sensors 20 (2020) 75, https://doi.org/10.3390/s20164484.
[38] L. Zhao, S. Wong, J. Sim, et al., Triboelectric nanogenerators and piezoelectric nanogenerators for preventing and treating heart diseases, BMEMat 1 (2023) 25, https://doi.org/10.1002/bmm2.12020.
[39] Y. Wu, Z. Liu, Y. Fan, Biomedical applications of bioresorbable mechanical sensors, Adv. Funct. Mater. 27 (2025), https://doi.org/10.1002/adfm.202513422.
[40] Y. Shan, E. Wang, X. Cui, et al., A biodegradable piezoelectric sensor for real-time evaluation of the motor function recovery after nerve injury, Adv. Funct. Mater. 34 (2024) 11, https://doi.org/10.1002/adfm.202400295.
[41] H. Zhou, Y. Zhang, Y. Qiu, et al., Stretchable piezoelectric energy harvesters and self-powered sensors for wearable and implantable devices, Biosens. Bioelectron. 168 (2020) 20, https://doi.org/10.1016/j.bios.2020.112569.
[42] L. Jiang, Y. Yang, R. Chen, et al., Flexible piezoelectric ultrasonic energy harvester array for bio-implantable wireless generator, Nano Energy 56 (2019) 216–224, https://doi.org/10.1016/j.nanoen.2018.11.052.
[43] X.Q. Huo, S.J. Luo, Z. Cao, et al., An implantable sensor based on shape memory polymers and triboelectric nanogenerators: monitoring ureteral peristalsis to assess bladder volume, Chem. Eng. J. 497 (2024) 10, https://doi.org/10.1016/j.cej.2024.154971.
[44] Y.S. Shi, S.H. Tang, W.F. Zhang, et al., A reliable, battery-free and implantable magnetic sensing system for wireless monitoring of spinal motion in rats and humans, Chem. Eng. J. 482 (2024) 10, https://doi.org/10.1016/j.cej.2024.148891.
[45] A. Shen, H.X. Xuan, Y.J. Jia, et al., Dynamic healing-assembly for biocompatible, biodegradable, stretchable and self-healing triboelectric nanogenerators, Chem. Eng. J. 491 (2024) 11, https://doi.org/10.1016/j.cej.2024.151896.
[46] X. Shi, Y. Sun, D. Li, et al., Advances in wearable flexible piezoelectric energy harvesters: materials, structures, and fabrication, J. Mater. Sci.-Mater. Electron. 34 (2023), https://doi.org/10.1007/s10854-022-09536-4.
[47] Y. Gu, T. Zhang, H. Chen, et al., Mini review on flexible and wearable electronics for monitoring human health information, Nanoscale Res. Lett. 14 (15) (2019), https://doi.org/10.1186/s11671-019-3084-x.
[48] F. Sheng, B. Zhang, Y. Zhang, et al., Ultrastretchable Organogel/silicone Fiber-helical sensors for self-powered implantable ligament strain monitoring, ACS Nano 16 (2022) 10958–10967, https://doi.org/10.1021/acsnano.2c03365.
[49] X. Hui, L. Tang, D. Zhang, et al., Acoustically enhanced triboelectric stethoscope for ultrasensitive cardiac sounds sensing and disease diagnosis, Adv. Mater. 36 (9) (2024), https://doi.org/10.1002/adma.202401508.